Deep learning for high-throughput quantification of oligodendrocyte ensheathment: a UNet architecture to extract multiple morphological parameters from individual cells

Yu Kang T Xu[1], Daryan Chitsaz[1], Robert A Brown[1], Qiao Ling Cui[1], Matthew A Dabarno[1], Jack P Antel[1], and Timothy E Kennedy[1]

[1]Department of Neurology and Neurosurgery, Montreal Neurological Institute, McGill University
timothy.kennedy@mcgill.ca - Corresponding author

ABSTRACT

High-throughput quantification of oligodendrocyte (OL) myelination is a significant challenge that impedes the development of therapeutics to promote myelin protection or repair. Here, we established classic algorithmic and deep learning approaches to quantify myelin in a nanofiber culture system. The classic algorithm was developed by modeling general characteristics of OL ensheathments, while the deep learning neural network employed a UNet architecture that enhanced its capacity to associate ensheathed segments with individual OLs. Reliably extracting multiple morphological parameters from individual cells, without heuristic approximations, significantly improved the validity of the neural network as this mimics the high-level decision-making capacity of human researchers. Experimental validation demonstrated that the deep learning approach matched the accuracy of expert-human measurements of the length and number of myelin segments per cell. The combined use of automated imaging and analysis eliminates weeks of manual labor while reducing variability to increase reliability when screening libraries of compounds. The capacity of this technology to perform multi-parametric analysis at the level of individual cells permits the detection of nuanced cellular differences to accelerate the discovery of new insight into OL physiology.

Keywords Image analysis · Oligodendrocytes · Deep learning · High-throughput screening

1 Introduction

In the CNS, oligodendrocyte (OLs) produce myelin by wrapping specialized multi-lamellar sheaths of membrane around axons. In pathological conditions, like multiple sclerosis, CNS trauma, or leukodystrophies, there is loss of myelin with inadequate replacement or repair of damaged sheaths [1]. Enhancing myelin production and stability are critical clinical objectives, and many in vitro systems have been established to study these dynamic processes. Dispersed cell cultures, for example, are often used to assess OL differentiation and membrane elaboration [2], whereas OL-neuron co-cultures are used to study myelination, as ensheathments formed on cultured axons have similar morphological characteristics to those observed in vivo [3, 4]. Recent advances in microfabrication have improved the reproducibility and throughput of in vitro myelination assays. One approach takes advantage of electrospinning techniques to culture OLs on axon-diameter polymer nanofibers. Initial contact involves OLs at an immature O4+ stage, followed by differentiation and expression of late antigens, like myelin-basic protein (MBP) [5]. The extent of ensheathment around these axon-like structures can be measured in response to different treatments, ranging from substrate coatings to the application of bioactive small molecules [6, 7, 8, 9]. Despite the variety of available cell culture strategies, OL myelination is typically quantified manually, creating a significant bottleneck and introducing human subjectivity into the analysis.

To resolve this quantitative challenge, we developed a combination of micro-engineered culture devices, automated imaging, and computational techniques for high-throughput extraction of the detailed morphological properties of individual OLs. We established these quantitative methods in a nanofiber culture system, consisting of commercially available 2 μm-diameter poly-L-lactic acid fibers spun onto the base of 96-well plates, as such nanofiber assays recapitulate biologically significant features of myelin development [6, 7]. The parallel arrangement of fibers in this assay facilitated the development of our two analytic systems: a classic algorithmic approach and a deep learning

neural network, both of which quantified immunocytochemically labelled markers of OL processes, such as sulfatides recognized by the O4 antibody, and MBP.

Our initial algorithmic approach modeled the general morphological characteristics of OL ensheathments, such as the presence of thick elongated structures. While this provided rapid analysis, the system only mimicked a single-cell level of analysis by using the location of nuclei within MBP stains to identify cell bodies, and the continuity of fluorescence to associate ensheathments to specific cells. This approximation of ensheathed OLs using a simplified distance measure and a linear-object filter limited the algorithm's capacity to reliably identify OL ensheathments on a cell-by-cell level.

To improve on the initial approach, we developed a deep learning technique with an enhanced capacity to rapidly extract multiple morphological parameters from individual OLs. Quantifying information at this single-cell resolution, without heuristic approximations, more closely resembles human analytic capacity and significantly increased the accuracy and validity of our approach. To establish a more reliable cell-by-cell analysis, our deep-learning technique employed a convolutional neural network (CNN) with a "UNet" architecture that was able to learn spatial and object-specific information [10]. Validation demonstrated that the deep-learning approach performed within the analytic range of human experts on multiple parameters (including length distributions and number of sheaths per cell), reduced work-loads, and provided standardization to decrease human variability. We also demonstrate the sensitivity of both systems to detect a pre-established biological difference between poly-D-lysine (PDL) and laminin-β1-coated nanofibers [7], with the latter increasing the number of sheaths formed per cell without significantly increasing the distribution of ensheathment lengths. These results highlight the capacity of this analytic approach to extract multiple morphological parameters and compare the effects of various manipulations on nuanced cellular processes.

Overall, these automated systems can image and analyze almost the entire surface of 96-well plates within 40 hrs using commercially available microscopy systems and graphics cards. Analytic speed can be further increased with parallel computing stations. By extracting multiple morphological parameters at single-cell resolution, while obtaining analytic quality similar to human segmentations, this high-throughput system can accelerate the discovery of therapeutics that promote myelin protection and improve our understanding of OL physiology.

2 Materials and Methods

2.1 Isolation and culture of primary rat oligodendrocytes

All procedures were performed in accordance with the Canadian Council on Animal Care guidelines for the use of animals in research and approved by the Montreal Neurological Institute Animal Care Committee and the McGill Animal Compliance Office. OL isolation was adapted from Lee et al. 2012. Briefly, P2 Sprague-Dawley rat brains were isolated by dissection in ice cold HBSS, the meninges removed, and cortices isolated. These were minced and digested at 37°C in 0.025% trypsin-EDTA and 0.2 mg/mL DNAseI for 20 and 3 min respectively. Dissociated cells were plated in PDL-coated T75 flasks (5 μg/mL) in DMEM containing 10% FBS and 1% pen/strep, and cultured for 2-3 weeks at 37°C with 5% CO2 and full media changes every 2 days. In these conditions, glial populations rapidly expand, permitting their isolation from other cell types based on differential adhesion. Media in the flask was replaced with 37°C 0.01% trypsin-EDTA in HBSS for 5 min, then swirled and aspirated to remove weakly-adherent microglia. DMEM was then added and the flasks vigorously hit 20 times with a styrofoam box. This mechanical agitation detached oligodendrocyte precursor cells (OPCs) while leaving most astrocytes attached. The media-cell suspension was plated in uncoated Petri dishes and incubated for 30 min to further purify the cells [6, 11], as astrocytes and microglia adhere more readily than OPCs. The OPC-containing supernatant was then collected and centrifuged for 5 min at 677 x g using a swinging bucket Centra CL2 centrifuge (Thermo), resuspended in Sato media (below), and triturated through 18 and then 22 gauge needles. The suspension was strained through a 70 μm filter, stained with Trypan blue to assess viability, and counted using a haemocytometer.

2.2 Electrospun nanofiber cultures and staining

96-well plates containing parallel aligned poly-L-lactic acid fibers approximately 2 μm in diameter (The Electrospinning Company) were soaked in 20% EtOH for 5 min, washed with HBSS, then washed twice with water and dried. Wells were coated with 5 μg/mL of FITC-labelled PLL in PBS for 1 hr at room temperature (RT, approximately 20°C), followed by 2 hr at 37°C with 10 μg/mL recombinant laminin-β1 in HBSS (Sigma). OL progenitor cells were seeded at 6000 cells per well in 100 μL of modified OL defined media to induce differentiation (DMEM, 5 μg/ml insulin, 100 μg/ml transferrin, 30 nM sodium selenite, 30 nM triiodothyronine, 6.3 ng/ml progesterone, 16 μg/ml putrescine, 100 U/ml penicillin, 100 μg/ml streptomycin, and 2 mM glutamax), as described [12]. For O4 antibody based studies, cells were kept in culture for 7 days and media was changed every 2 days. For MBP based studies, cells were kept in culture for 14 days; and media was half-changed every 4 days. After the stated culture period, live cells were then incubated with the O4 antibody for 15 min at 37°C and then fixed by adding 100 μL of chilled 4% paraformaldehyde in 20% sucrose for 15 min at RT. For MBP staining, fixed cells were blocked and permeabilized for 15 min with 5%

HINHS (heat-inactivated normal horse serum) in 0.1% Triton X-100 at RT, and then incubated with a primary chicken anti-MBP antibody in 5% HINHS (1:1000; Aves labs) for 4 hr at RT. The OLs were then washed in PBS before being incubated with IgM Cy3, for O4 stained cells, or Alexa-546 conjugated goat anti-chicken secondary antibody (1:1000; Molecular Probes), for anti-MBP stained cells, in addition to 1 μg/mL of DNA staining Hoechst 33342 (Sigma) for 2 hr at RT in 5% HINHS. Cells were washed again with PBS and kept at 4°C until they were imaged.

2.3 Automated Imaging

Nanofiber plates were imaged using an LSM 880 inverted confocal laser scanning microscope (Carl Zeiss) with a 10X (NA 0.45) Plan-Apochromat objective. Since the excitation and emission peaks of our dyes differed by > 100 nm, it was possible to acquire both on a single track with no bleed-through, saving considerable time. Acquisitions were automated using Zen Black Systems v2.3 and the Tiles and Positions software module, such that the user is only required to set the PMT gain to account for differences in staining intensity between experiments, and calibrate the motorized stage to target the center of the first well of each plate. In 16 hrs of acquisition, the system imaged $\sim 4 \times 4$ frames centered in the middle of each well to cover a $\sim 4 \times 4$ mm area with a pixel resolution of 0.5 μm, thereby acquiring >50% of every well with no bias. Focus was performed automatically for each well with the DefiniteFocus.2 module. Since the nanofibers are not perfectly planar, three to five confocal slices covering 10-20 μm in the Z-dimension were acquired for each frame to ensure that all cells were sampled. At lower resolutions, each well took < 10 min to acquire, allowing the whole plate to be imaged in less than 16 hrs. Z-stacks were stitched and compressed via the Extended Depth of Focus (maximum projection) algorithm in Zen Black prior to exporting the images as TIFF files.

2.4 Manual segmentation criteria

A set of criteria was defined for classification of "ensheathed" OLs based on morphological characteristics identified using Hoechst, O4, and MBP staining: (1) The presence of an identifiable cell body and nucleus. (2) The presence of ensheathed processes, defined as segments of O4 or MBP running parallel to the nanofibers in the culture plate having a length > 12 μm and a thickness > 2 μm. (3) Continuation of the cell body with the ensheathments. (4) Each ensheathed fiber may only be associated with 1 cell nucleus. Human researchers were given these criteria and instructed to trace the border of OL ensheathments using the ImageJ polygon tool. These manual segmentations were then used to train and validate our deep learning network.

2.5 Classic algorithmic MATLAB segmentation

A classic algorithm was first constructed to implement our manual segmentation criteria. To fulfill criteria 1, cell bodies were identified through colocalization of Hoechst stained nuclei with MBP-positive cytoplasm. To separate overlapping and crowded cell bodies, the local maxima of a distance transformed MBP image was used for watershed segmentation. For criteria 2, after convolution with second derivative Gaussian filters, ensheathed nanofibers were segmented using a ridge-filter that extracts the eigenvalues from the Hessian matrix of the MBP image. The sensitivity of segmentation was user specified and the diameter of fibers segmented could be modified by altering the sigma of the initial Gaussian filters. The algorithm then cycled through each cell body to associate segmented fibers with corresponding nuclei, thereby satisfying criteria 3 and 4 (Figure 1A). An important disadvantage of this classic algorithmic approach is that the identification of ensheathments and the association of segments to individual cells is performed as two separate quantitative steps. The ridge-filter is applied to extract ensheathments globally from an image and then the local distance maxima of cell bodies is used to associate those segments to individual OLs to mimic a cell-by-cell level of quantification (Figure 1A). By separating the analysis into two streams, however, the algorithm is not capable of performing the high-level decisions required to reliably associate ensheathments to cells when faced with over-crowded images or when fluorescent staining is faded. The deep learning approach overcomes these challenges by using spatial and object-specific information simultaneously to analyze and associate OL ensheathments with a specific cell.

2.6 Neural network training data

To train a neural network to extract morphological features from individual OLs, we generated 3-channel images for our input data, with the middle channel replaced by a mask over a specific nucleus of interest (Figure 2A). This mask prompted the network to learn to associate OL ensheathments with individually masked nuclei. The input data was also appended with a ground-truth image, containing the human tracings of OL ensheathments. To create the ground-truth images, human researchers: (1) manually traced a single cell nucleus with its corresponding ensheathments, saved that as an ROI file in ImageJ, and then repeated the process for every cell in a whole-well image. (2) The ROIs were then used to generate two 16-bit images, one containing all the manually traced nuclei, and the other containing all the manually traced ensheathments. (3) A Python script then looped through the nuclei-containing image, using each nucleus as a center to crop/create input and ground-truth images for every cell in a full-well image. Cropping

input data from individual cell nuclei significantly increased the number of training images, generating $\sim 40,000$ input examples from a dozen full-well images.

2.7 Neural Network Architecture

Google's open source Tensorflow [13] was used to implement a CNN with a "UNet" architecture [10]. The U-shaped design was selected for its capacity to learn to associate ensheathments to individual OLs, as the down-sampling arm of the network learns features at a variety of scales, and the up-sampling arm combines spatial information from earlier layers to produce a high resolution final segmentation (Figure 2B). The down-sampling branch contained 5 two-dimensional convolutional layers with $\sim 5 \times 5$ pixel kernels and a stride of 2. The number of filters at each subsequent layer increased by 10 sequentially from 10 to 50. The up-sampling branch of the network was symmetric to the down-sampling branch but used fractional strides to up-sample the information back to the original size. The up-sampling convolutional layers had $\sim 5 \times 5$ pixel kernels and a decreasing number of filters that dropped sequentially by 10 from 50 to 10. The up-sampling branch also mixed in spatial information by concatenating data from earlier layers with similar resolution prior to each convolution. The output of the up-sampling branch was then passed through a softmax convolutional layer with a $\sim 1 \times 1$ pixel kernel to generate two mutually exclusive probabilistic output categories corresponding to background and fibers. This probabilistic output was then thresholded at a value of 0.5 to produce a binary segmentation that contains the ensheathments identified by the network for a single cell.

2.8 Implementation and pre-processing of CNN analysis

All resources in this paper will be made freely available through deepdiscovery.org. Python and Tensorflow must be pre-installed before running the CNN package. Once the files are in a local directory, the user runs the "main" file in Python and is prompted to select an input folder which should contain single RGB images of any size. The user must input a few manual parameters (resolution of the image, minimum length criterion, and minimum nucleus size), before the program begins the analysis. An image first undergoes pre-processing by watershed segmentation to identify Hoechst stained nuclei. These nuclei are then used to generate "input" images, where the middle channel is replaced with a masked array over a nucleus of interest so the network can perform segmentations specific to individual OLs (Figure 2A). To avoid redundancy, we recognized that there are cells lacking any ensheathed segments—defined as having nearly zero O4 or MBP near the cell nucleus. Such cells are identified and excluded to save analytic time by binarizing the O4 or MBP channel followed by morphological closing then opening to generate blobs. Only nuclei within O4 or MBP blobs were considered "candidates" for quantification, thus avoiding analysis of cells that are clearly MBP negative.

2.9 Post-processing after CNN analysis

After the network cycles through each "candidate" cell within a full-well image, we applied three post-processing steps to assign "overlapped" ensheathments—associated to more than one cell—while removing "sticky" connections (see below) and setting a minimum threshold for ensheathment length (Figure 2B):

1. ***Method of unfair distribution:*** Given the choice to assign an ambiguous "overlapped" ensheathment to a large cell with multiple ensheathed nanofibers, or a small cell with only a single ensheathment, this method operates under the assumption that it is more likely that the uncertain segment will belong to the larger cell.
2. ***Sticky-removal:*** To separate "sticky-segments"—adjacent ensheathments that touch and are wrongly identified as a single object—the method skeletonized the output image and removed all branch points. It then cycled through all the broken segments to eliminate any that were horizontal. Branch points were then re-inserted to restore the vertical connectivity of the ensheathments without their "sticky" horizontal connections.
3. ***User-specified min-length:*** Ensheathments below a minimum length (~ 12 μm) were eliminated. As well, since we noticed slight over-sensitivity toward cells with only one or two ensheathments in human non-experts and machines, we also programmed a sensitivity measure to reduce variability across experiments. We recommend a length threshold that is 3–4 times more strict for those single and doubly-ensheathed cells to reduce the chance of identifying false positives, but this value can be adjusted to suit the researcher's needs. Length was determined by fitting the objects with an ellipse and calculating the distance of the major axis, as defined in regionprops OpenCV [14].

2.10 Training

A total of $\sim 40,000$ input images were cropped from full-well images to train the neural network. 1,111 of these cropped images were utilized for validation during training, which allowed us to follow the performance of the model as it learned. After training was performed for 350,000 epochs (about 6 days) on an NVIDIA Tesla P100-PCIE, one entire whole-well image (containing 1,667 input cells traced by a human researcher) was used to test the network for

its performance on global parameters and generalizability to new data. The cost function driving the training process was the categorical cross-entropy, on a per-pixel basis, between the output of the network and the manual segmentation. To improve the rate of learning and the sensitivity of the network for the edges of objects, the cost function was also weighted by an exponential decay formula:

$$w = e^{1-\frac{D}{f}+b}$$

where W refers to the weighted loss at each pixel, f modifies the rate of falloff from the edge, and b prevents the weights from reaching zero. D is the distance from the edge of the OL ensheathments, calculated by computing the Chebyshev distance transform of the inverted ground-truth mask. Overall, this formula weights the training loss such that it decays exponentially with distance from the margins of the ensheathed segments of interest, thus helping the network "focus" on correctly identifying the edges of objects (Figure 3E). A second neural network was also trained using a class weight of 10 for comparison. Class weighting was implemented to better balance the dataset, as only a minority of the single-cell images in the training data were ensheathed cells.

3 Results

To resolve the analytical challenge posed by high-throughput quantification of OL ensheathments, we first developed a classic algorithm that was modeled after two primary morphological properties: linear segments and continuity with cell bodies. The significance of these features for image analysis were established based on higher resolution images of OL nanofiber cultures, and then approximated by MATLAB software using a ridge-filter and watershed segmentation (Figure 1A - B). Despite qualitatively valid segmentations and a rapid analysis for the nanofiber system (Figure 1B), we realized that this approach could not fully match human analytic accuracy as the algorithm used heuristic approximations, like linearity and local distance maxima, to associate ensheathed segments to individual nuclei. To improve beyond the preliminary model, we developed a deep-learning approach with an enhanced capacity to associate multiple-morphological features with specific OLs.

To train a deep learning model to match the cell-by-cell analysis performed by human researchers, we presented the network with $\sim 40,000$ input images that each contained a masked nucleus of interest (Figure 2A - B). The performance of our CNN in task-learning was monitored through the loss value and Jaccard index (JI). Categorical cross entropy was used as our loss function, as it measured the difference between the CNN output and the manually traced ensheathments generated by an experienced cell biologist (ground truth). The JI, on the other hand, was used to measure the overlap similarity between the binarized output of the CNN and the ground-truth [15]. In our model, a decrease in loss and increase in JI, calculated on a validation set of 1,111 images, served as an indicator for successful task-learning and the generalizability of the network to new data (Figure 3A - B).

During training, we weighted the loss function of CNNs to penalize mistakes in different ways to promote learning. Class weighting was used to emphasize decisions about ensheathments by a factor of 10, whereas spatial weighting was used to penalize decisions to emphasize the edges of objects (Figure 3E). Although both weighting schemes dramatically improved CNN performance, indicated by an earlier and steeper increase in JI, the spatially weighted network was superior, as it's JI continued to improve while the class weighted network plateaued at $\sim 180,000$ training epochs (Figure 3B). Using these parameters, along with testing at progressive checkpoints, we found the best model was generated at $\sim 301,000$ epochs by the spatially weighted network (Figure 3A). Furthermore, by plotting the output of select layers of this spatially weighted model, we visually confirmed that the network had learned to associate ensheathments to individual masked OLs (Figure 3C - D). Combining spatial and object-specific information to reliably analyze single cells without heuristic approximations illustrates a key advantage of the deep learning technique over classic algorithmic segmentations.

After generating our classic algorithm and deep-learning models, we evaluated the performance of both systems in relation to human scientists. Three human researchers were employed for this analysis and were ranked by their experience with OL cultures—human 1 (H1) being a cell biologist, H2 a computer-scientist, and H3 a summer medical student. On a whole image level, the output of machines on the test image (1,667 candidate cells) fell within the range of human quantification on multiple parameters (Figure 4). No statistically significant differences were detected between the log and absolute mean fiber lengths between all human and machine analysts (Figure 4A - B). Despite having clear criteria as to what constitutes an ensheathment, variability between humans was much higher when quantifying the number of sheaths formed per cell (Figure 4C). Only the CNN successfully identified a mean number of sheaths per cell that did not differ significantly from the expert counter H1 (Figure 4C). The overall number of ensheathed cells identified was also fairly consistent between groups, except for H2, emphasizing again the inherent variability in counting among humans and the advantage of using a computational approach to standardize methodology (Figure 4D).

After evaluating global parameters, we compared the ability for both models to match human analysis on a cell-to-cell level. To assess the performance of all models on individual cells, we selected H1 as ground-truth and computed the JI for every cell that was commonly identified after pairing H1 with each researcher or computer program. We

found that the CNN outperformed human participants and the classic algorithm in matching H1 at single-cell resolution (Figure 4E). We also computed a global JI for the entire whole-well image and found that the CNN best matched expert H1 (Figure 4F). Thus, the CNN outperforms the classic algorithm in analysis at single-cell resolution and in global parameters due to its heightened capacity to extract information from individual OLs.

Having validated the models on both whole-image and cell-to-cell levels, we assessed the capacity of the algorithms to detect a subtle biological effect by examining the difference between PDL and laminin-$\beta 1$ coated nanofibers [7]. Compared to PDL coatings, laminin has been shown to increase the number of sheaths formed per cell without significantly influencing the distribution of ensheathment lengths [7]. Both machine programs recapitulated those findings. For the number of sheaths formed per cell, the classic algorithm found a difference of 0.96 ± 0.17 sheaths ($p < 0.0001$) and the CNN found a difference of 0.47 ± 0.11 sheaths ($p < 0.0001$) between laminin and PDL coated conditions (Figure 5C). For log length distributions, both the classic algorithm and the CNN identified a very small but statistically significant difference in means of 0.022 ± 0.0038 ($p < 0.0001$) and 0.016 ± 0.0054 ($p = 0.004$) log units respectively (Figure 5A - B). While Bechler et al. [7] only observed a non-significant upwards trend in the lower and upper bounds of the log length distribution in laminin coated conditions, our results demonstrated an added advantage of our high-throughput systems: by sampling ~ 25 times more ensheathments in each experimental condition (~ 8000 instead of ~ 300 ensheathments), we detected a significant difference between extraordinarily nuanced biological effects. This assessment verified the sensitivity of our systems and highlights the importance of evaluating multiple morphological parameters when assessing differences in the capacity to form myelin-like wraps.

Finally, we evaluated the speed of our models for practical use. Using an Intel Core i7 processor, the automated algorithms reduced the analytic time from a projection of ~ 26.7 days for manual human quantification (of one 96-well plate) to ~ 1.3 days for the classic algorithm and ~ 3.3 days for the CNN. Using an NVIDIA GTX 1070 graphics card, however, the speed of analysis for the CNN outperformed the classic algorithmic approach by analyzing 96 wells in ~ 1 day (Table 1). Automated imaging reduced the time for image-acquisition by about $\sim 50\%$ (Table 2), and the entire pipeline dramatically enhanced the speed of analysis while almost eliminating manual-labor, thus providing the capacity to screen hundreds of compounds within a week.

4 Discussion

To address the need for high-throughput systems that can quantify multiple morphological properties of OLs and associate them with specific cells, we developed two computer-vision strategies that work in conjunction with automated imaging and nanofiber cultures. We demonstrate that the deep learning system has the capacity to detect finely nuanced biological differences and to match the quality of quantification carried out by a human expert.

The biological and computational techniques employed both have unique advantages and limitations. The reduced complexity of the nanofiber culture system, which lacks axons and other factors that can influence sheath stability and extension [16, 17, 18], is critically advantageous to isolate OL intrinsic responses while also substantially increasing the reproducibility of quantification for high-throughput screening. OLs cultured on nanofibers broadly recapitulate the temporal and spatial progression of differentiation seen in vivo [6], forming compact myelin-like MBP positive layered sheaths on nanofibers [7]. As well, the parallel arrangement of the nanofibers significantly facilitated the development of our analytic programs, as it was not necessary to overcome the challenge of identifying and associating myelin-like sheaths that cross-over one another, as occurs in typical axon-OL co-cultures. A final advantage of the nanofiber system is that it facilitates the assessment of multiple biologically relevant parameters, such as the number sheaths formed per cell, the distribution of sheath lengths and widths, and the proportion of cells that form ensheathments [2, 19]. Access to quantitative information for multiple parameters per cell is a significant advantage to infer and ultimately identify which cellular process is affected by any given treatment. For example, changes in the number of ensheathed cells implies an effect on OPC proliferation/differentiation, whereas changes in sheath lengths would suggest altered process extension or stabilization. In contrast, conventional high-throughput screens typically reduce individual wells to a binary fluorescent signal, which loses information pertaining to specific cellular dynamics. The system we describe here is a unique tool that rapidly extracts multiple parameters to detect nuanced physiological processes that can then be further studied in more complex systems.

The two computational approaches presented offer several advantages beyond reducing human workloads and extracting multiple morphological features. For example, both the classic algorithm and CNN have set parameters that allow for standardization across experiments to reduce human error. As well, since these programs are computer-based and the task is highly parallelizable, analytic speed can be enhanced nearly indefinitely by employing parallel computing workstations and GPUs. Limiting factors are the cost involved and the time for sample preparation. Notably, the ability of the CNN to run in reasonable time on common CPUs is attributable to the great reduction in neural network size. Compared to the original UNet architecture proposed by Ronneberger et al., which scaled to 1024 filters in the deepest layers, our network is computationally more efficient, scaling to only 50 filters in the deepest layer.

Aside from similar advantages, the two programs differed in their accuracy and speed. With regard to accuracy, the classic algorithmic approach is unable to offer an extremely reliable analysis as it uses computational approxi-

mations to extract global parameters from an image and then attempts to mimic cell-by-cell analysis by associating ensheathments with nearby nuclei. On the other hand, the CNN offered a more "human-like" assessment of nanofibers since it learned to perform high-level decisions using spatial and object-specific information simultaneously to extract parameters from individual cells. Although the classic algorithm is less accurate, it is important to highlight that the approach is still consistent, fast, and responds more easily to user-specified parameters. Thus, the classic algorithm may find substantial utility as a relatively simple computational tool that can be quickly applied to a variety of OL-based imaging experiments that require detection of linear ensheathments.

A final consideration is the generalizability of these programs. While the classic algorithm was designed explicitly for aligned nanofiber cultures, it has the immediate capacity to analyze linear sheath-like objects in other imaging challenges. The major obstacle to this generalizability is that such an application may require a researcher to have programming experience to alter the program to fully suit their needs. In contrast, the CNN is able to match human segmentations on a variety of computational problems without enormously altering the algorithm. For example, given that our CNN performs well with evenly-distributed parallel sheaths in our nanofiber culture system, this quantitative approach could reasonably be applied to tissue sections from CNS regions that recapitulate an aligned geometry, like aligned white matter tracts in the optic nerve and spinal cord. By using sparse labelling strategies, such as in utero fluorescent reporter electroporation or immunohistochemical staining in regions lacking complete myelination, our neural network has the potential to quantify myelin-sheaths in tissue sections. The major limiting factor for generalizability with the CNN is the time required to re-train the network and to create ground-truth data for supervised learning. While training is ideally only performed once, and we trained the network with a variety of cell culture and imaging parameters, the full capacity of the CNN to generalize across larger variations in experimental preparations and imaging systems remains to be determined. A summary of key comparisons between programs is presented in Table 2.

5 Conclusion

In this study, we have developed a powerful paradigm for high-throughput screening of OL ensheathment through the combination of state-of-the-art deep learning technology and readily available imaging and cell culture systems. Our methods extract multiple morphological parameters from individual OLs, preserve human analytic quality, remove bias and variability, and massively increase sample size and analytic speed. These new developments promise to advance our understanding of fundamental OL physiology and accelerate the discovery of new drugs for the treatment of myelin diseases.

6 Acknowledgments

We thank Compute Canada for access to computer clusters to train the neural network, and Drs. Thomas Stroh and Liliana Pedraza at the Microscopy Core at the Montreal Neurological Institute for technical assistance. This research was undertaken thanks in part to funding from the Canada First Research Excellence Fund, awarded to McGill University for the Healthy Brains for Healthy Lives initiative. Additional support was provided by grants from the International Progressive Multiple Sclerosis Alliance (BRAVEinMS) and the Multiple Sclerosis Society of Canada.

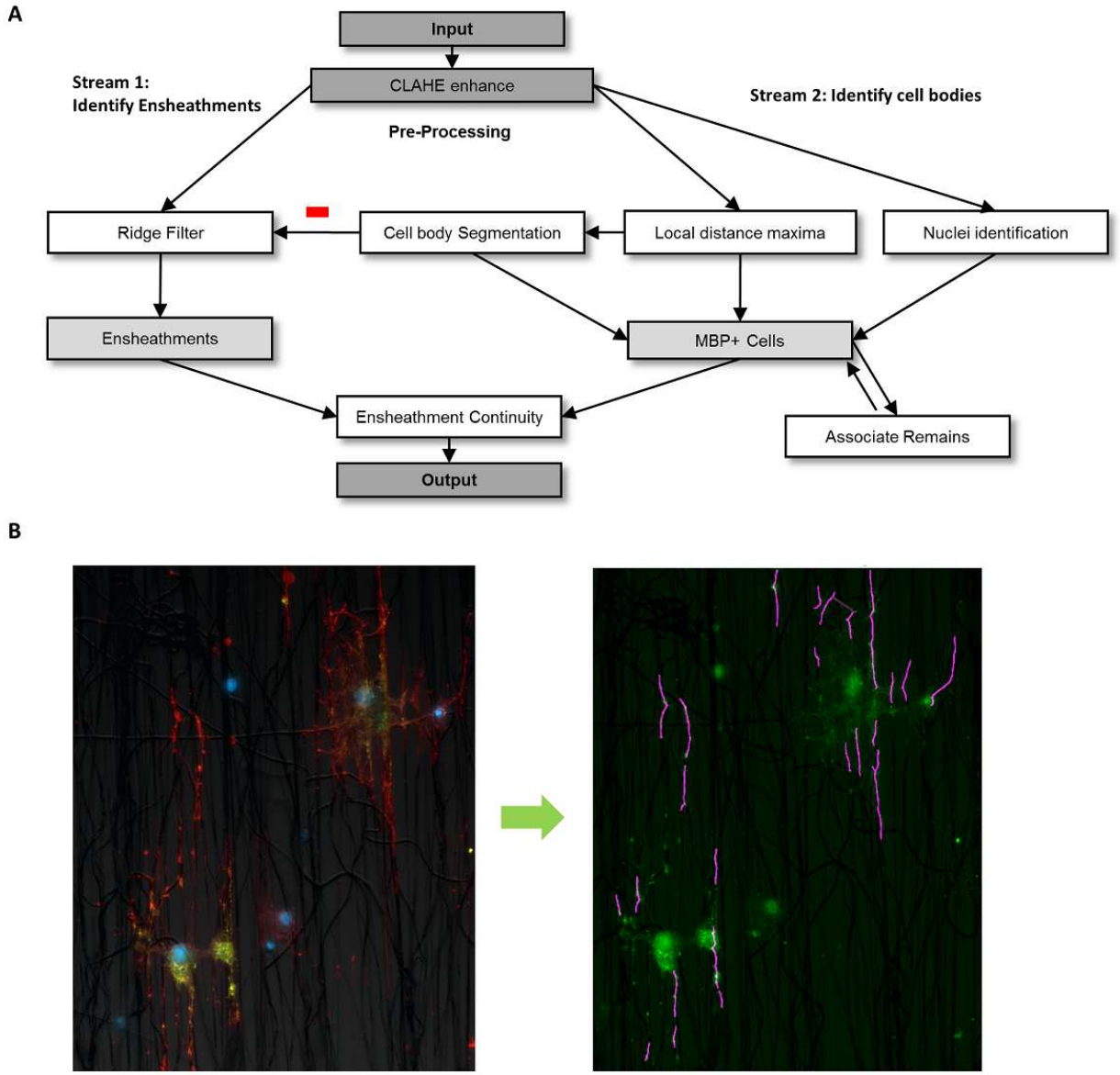

Figure 1: Classic MATLAB algorithm – ridge-filter for identifying ensheathed OLs. (A) Input images are pre-processed using CLAHE enhancement to increase contrast before identifying ensheathments and OL cell bodies in two separate analytic streams. (Stream 1) a ridge-filter is applied to identify ensheathed nanofiber segments and (Stream 2) cell-bodies are estimated using watershed segmentation with imposed local distance maxima. The middle link (red subtrac5ion sign) subtracts the cell bodies from the ensheathments identified by the ridge filter to eliminate segments located within cell bodies. The final outputs of both pathways are combined for ensheathment continuity analysis. (B) Input and output of the classic algorithmic approach. Cell nuclei (blue), O4 (red), MBP (green), nanofibers (bright field in background). Purple outlines in the "Output" image indicate the segmentations performed by the algorithm.

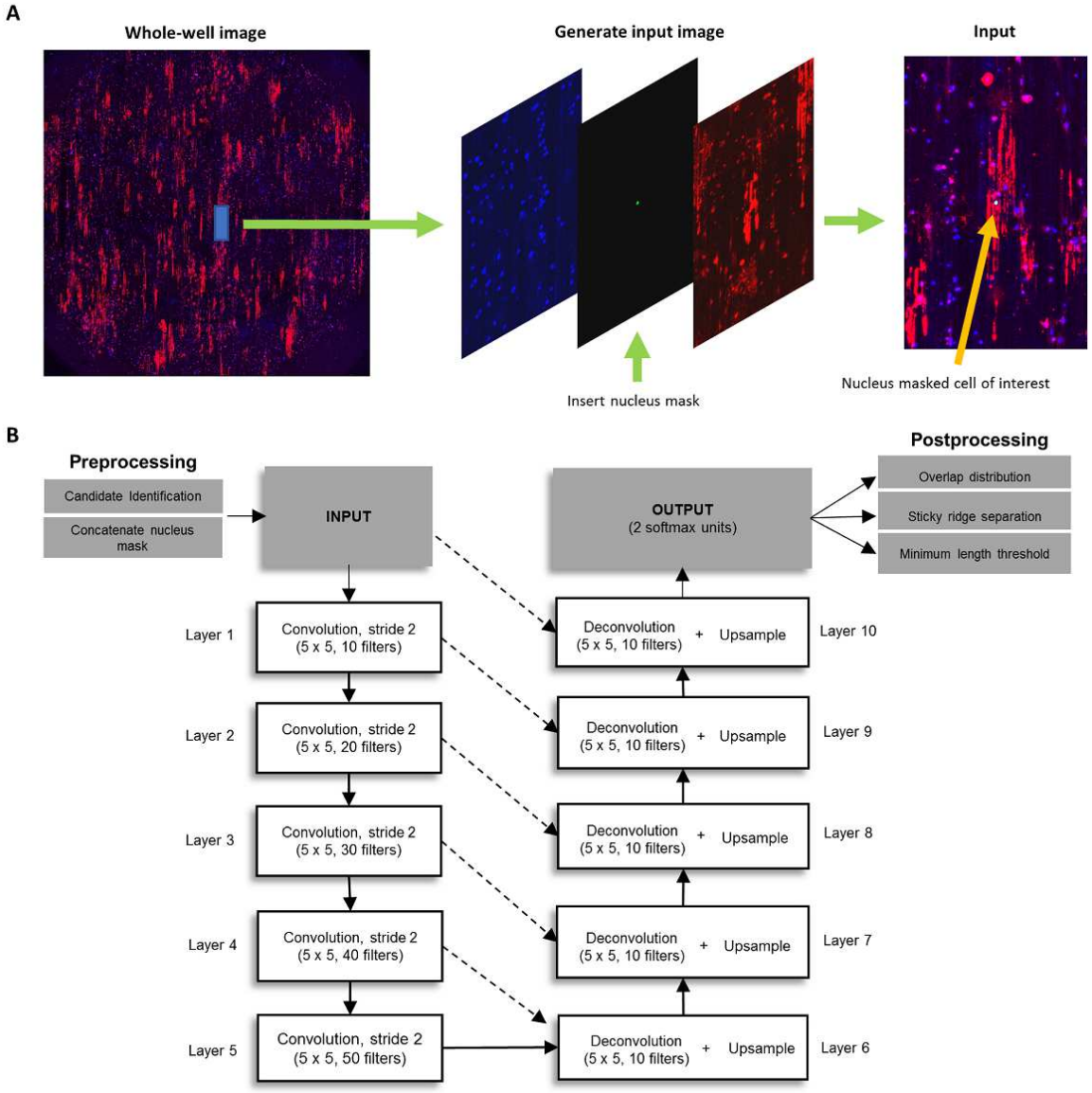

Figure 2: Pre-processing, network architecture and work-flow. (A) The blue rectangular mask on the whole-well image (left) indicates the portion of the image cropped around a candidate Hoechst center. That Hoechst center is then used as a mask to replace the green channel in the "Input" image (right). This method is used to generate both the training images and the input images when testing the algorithm. (B) Starting from the left, a whole-well image is pre-processed to generate nuclei masks for candidate cells. These candidates are then piped into the network architecture as an "input" image that is down-sampled on the left arm of the network, and then up-sampled on the right-arm of the network. Spatial information from the down-sampling branch is also mixed into the up-sampling branch to allow the network to learn to associate ensheathments to individual OLs. The final "output" segmentation is then subjected to further post-processing

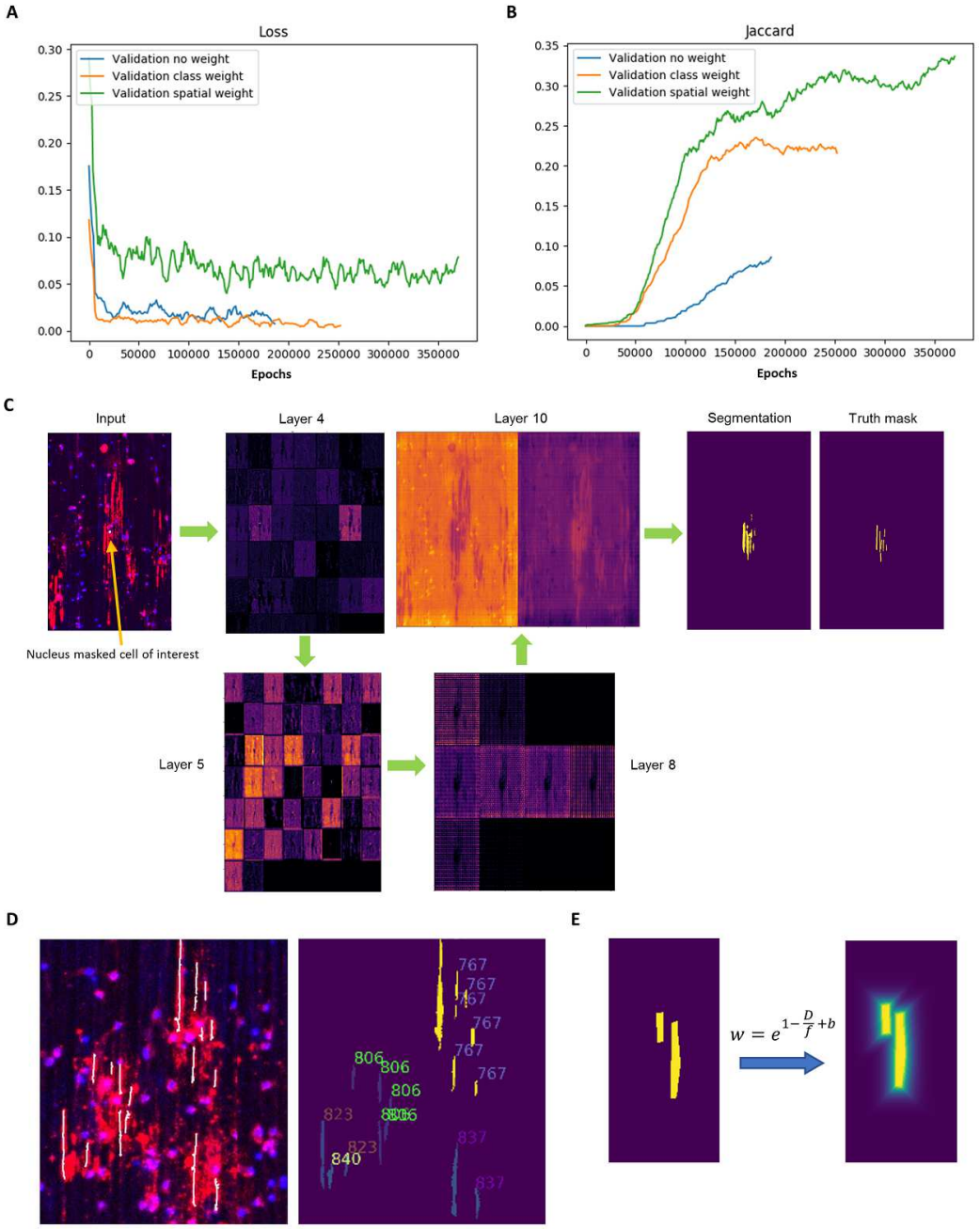

Figure 3: CNN training and demonstration of cell-specificity. (A) Loss decreased continuously for all validation sets, however, the spatially weighted network did see an increase in validation loss after $\sim 301,000$ epochs, indicating overfitting. Thus, the training was stopped early for testing. (B) Both class and spatial weighting improved learning rates dramatically, as indicated by an earlier and steeper increase in the JI of the validation sets. However, class weighting appears to plateau without an improvement in the JI after $\sim 180,000$ epochs. The spatially weighted CNN was therefore selected as our best model. (C) Sample outputs of specific layers leading to the final output "segmentation". "Layer 4" seemed to have a binary response to the distribution of MBP immunoreactivity, while "Layer 5" seemed to activate for different parts of the MBP image, suggesting the extraction of features corresponding to linear ensheathments. (D, left) Zoomed inset of the 10x whole-well image used for testing. The ensheathed fibers segmented by the UNet are overlaid (white). Hoechst is shown in blue and MBP in red. (D, right) Ensheathed fibers segmented by the UNet are annotated to indicate the specific cell that they belong to, showing that the network learned to associate fibers with specific nuclei, rather than identifying individual segments globally across a whole-image. (E) Illustration of the effects of spatial-weighting to draw "attention" to object edges during training.

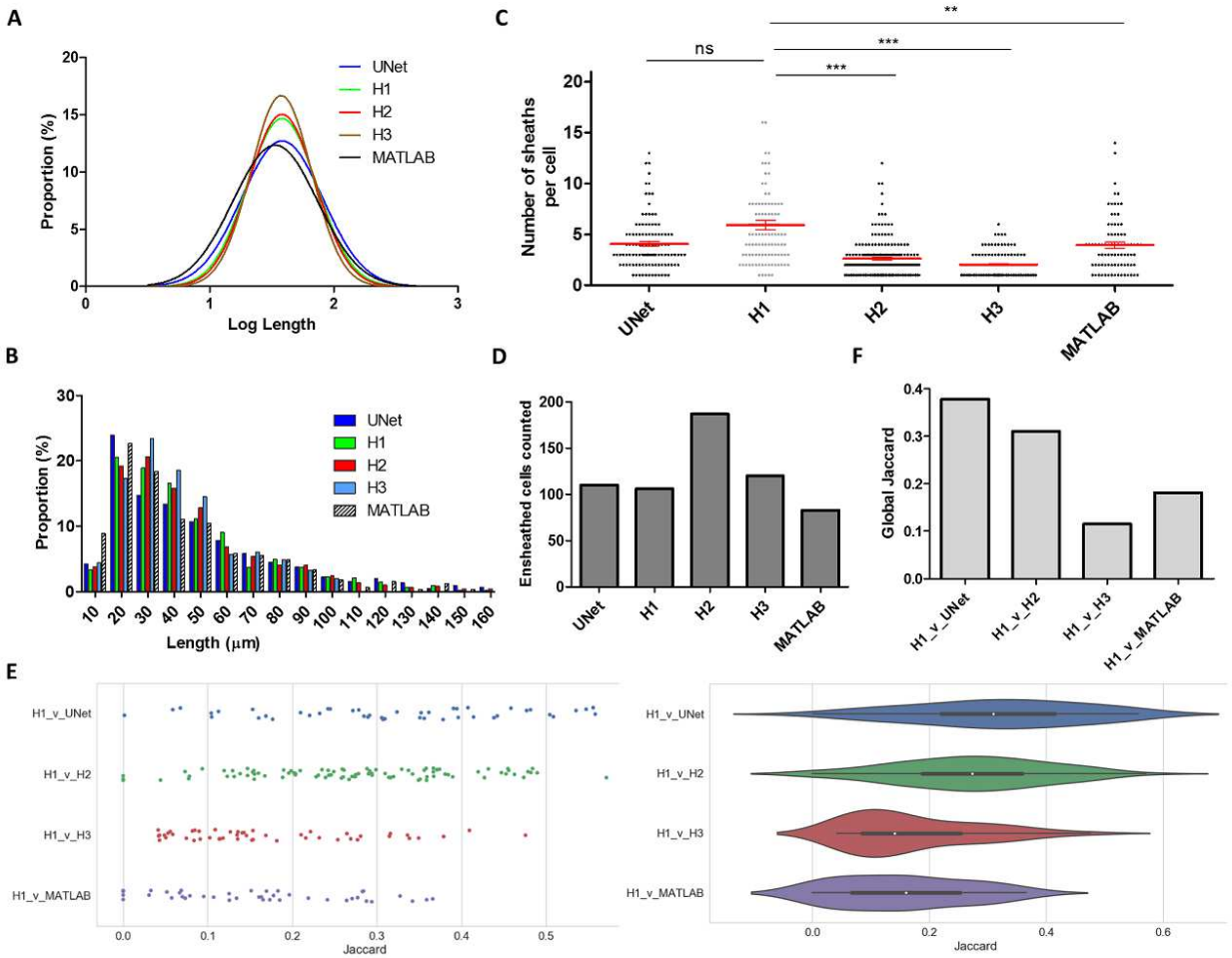

Figure 4: Comparison of the performance of humans (H1, H2, H3) and machines (UNet, MATLAB) on a whole-well image. (A) Log and (B) absolute distributions of ensheathment lengths are not significantly different between machines and humans with an average of 430 sheaths identified by each algorithm or researcher (one-way-ANOVA with Tukey's post-test). (C) Only the number of sheaths per cell identified by the UNet matched that of H1 (the expert). Other humans with less expertise, and the MATLAB program, differed significantly from H1 (Kruskal-Wallis test with Dunn's post-test). (D) The total number of ensheathed cells was identified similarly by all groups, except H2. This variability in analysis by human non-experts supports the need for standardized analytic systems. (E) Scatter and violin plots of single cell Jaccard values using Human 1 (H1) as the "ground-truth" compared with H2, H3, UNet, and the classic algorithmic approach. Overall, the UNet and H2 best matched the expert on a cell-to-cell basis. (F) Global Jaccard values were also computed across an entire whole-well image between the same comparison groups. The UNet and H2 again had the highest match with expert H1.

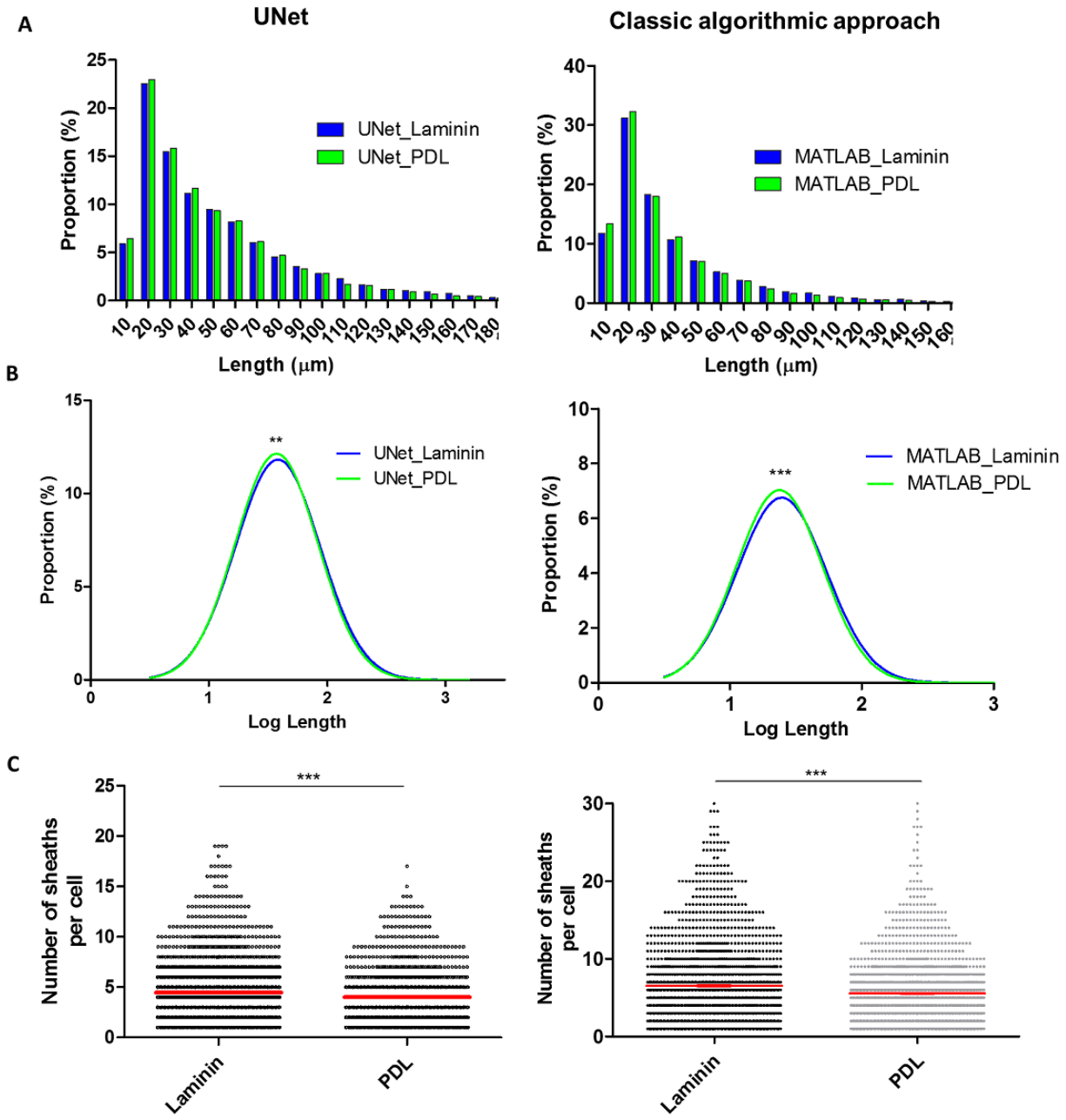

Figure 5: (A) Absolute and (B) log length distributions had a small but significant difference in means of 0.016 ± 0.0054 log units ($p = 0.004$, Student's T-test) as detected by the UNet, and a difference in means of 0.022 ± 0.0038 log units ($p < 0.0001$) as detected by the classic algorithmic approach for an average of 8000 sheaths in every condition. (C) Both systems detected increases in the number of sheaths formed per cell between laminin and PDL coated nanofibers. The UNet found a significant difference in means of 0.47 ± 0.11 sheaths ($p < 0.0001$, Mann-Whitney U-test), while the classic algorithmic approach identified a significant difference in means of 0.96 ± 0.17 sheaths ($p < 0.0001$) between the two conditions for an average of 1500 ensheathed cells in each condition.

Table 1: comparison of human and machine approaches for quantifying OL ensheathment

	Time per cell (seconds)	Time per well (mins)	Time 96 wells (days)****	Benefits	Limitations
Human	80	*400	∼26.7	- Adaptable - Fast learner	- Variable - slow and costly
MATLAB	-	**20	∼1.3	- Fast - Standardization - User customizability	- Approximates cell-by-cell analysis
UNet	1.5	***50	∼3.3	- Moderate-Fast speed - Adaptable given time to train - Standardization - Analysis at level of single-cells	- Training time long - Uncertain generalizability
UNet (GPU accelerated)	0.5	***15	∼1		

*assume ∼300 ensheathed cells per well
**program cuts whole-wells into 16 sections if insufficient memory, taking ∼1 minute on each section
***assume ∼2000 candidates per well
****analysis time similar for 384-well plates due to identical plate area

Table 2: comparison of imaging time. Automated imaging approach reduces manual labor significantly, while also reducing capture time due to automated focus and pre-defined acquisition area

	Time 96 wells (hours)	Benefits	Limitations
Manual Imaging	∼77*	- Able to selectively focus	- Extremely slow if imaging whole wells - biased by human field selection
Automated Imaging	∼16	- Whole-well imaging eliminates field selection bias - Fast	- Automated focus may not always focus on best stack

*16 fields with 4-5 z-stacks per well. Roughly 3 mins/field

References

[1] R. J. M. Franklin, "Why does remyelination fail in multiple sclerosis?," *Nature Reviews Neuroscience*, vol. 3, p. 705, 2002.

[2] A. A. Jarjour, H. Zhang, N. Bauer, C. Ffrench-Constant, and A. Williams, "In vitro modeling of central nervous system myelination and remyelination," *Glia*, vol. 60, no. 1, pp. 1–12, 2012. 1098-1136 Jarjour, Andrew A Zhang, Hui Bauer, Nina Ffrench-Constant, Charles Williams, Anna G0601744/Medical Research Council/United Kingdom G0901697/Medical Research Council/United Kingdom 083585/Wellcome Trust/United Kingdom Journal Article Research Support, Non-U.S. Gov't Review United States Glia. 2012 Jan;60(1):1-12. doi: 10.1002/glia.21231. Epub 2011 Aug 19.

[3] C. E. Thomson, M. McCulloch, A. Sorenson, S. C. Barnett, B. V. Seed, I. R. Griffiths, and M. McLaughlin, "Myelinated, synapsing cultures of murine spinal cord–validation as an in vitro model of the central nervous system," *Eur J Neurosci*, vol. 28, no. 8, pp. 1518–35, 2008. 1460-9568 Thomson, C E McCulloch, M Sorenson, A Barnett, S C Seed, B V Griffiths, I R McLaughlin, M 077089/Wellcome Trust/United Kingdom Wellcome Trust/United Kingdom Journal Article Research Support, Non-U.S. Gov't Validation Studies France Eur J Neurosci. 2008 Oct;28(8):1518-35. doi: 10.1111/j.1460-9568.2008.06415.x. Epub 2008 Sep 10.

[4] L. Stoppini, P. A. Buchs, and D. Muller, "A simple method for organotypic cultures of nervous tissue," *J Neurosci Methods*, vol. 37, no. 2, pp. 173–82, 1991. Stoppini, L Buchs, P A Muller, D Journal Article Research Support, Non-U.S. Gov't Netherlands J Neurosci Methods. 1991 Apr;37(2):173-82.

[5] R. Bansal, A. E. Warrington, A. L. Gard, B. Ranscht, and S. E. Pfeiffer, "Multiple and novel specificities of monoclonal antibodies o1, o4, and r-mab used in the analysis of oligodendrocyte development," *J Neurosci Res*, vol. 24, no. 4, pp. 548–57, 1989. Bansal, R Warrington, A E Gard, A L Ranscht, B Pfeiffer, S E NS10861/NS/NINDS NIH HHS/United States Journal Article Research Support, U.S. Gov't, P.H.S. United States J Neurosci Res. 1989 Dec;24(4):548-57. doi: 10.1002/jnr.490240413.

[6] S. Lee, M. K. Leach, S. A. Redmond, S. Y. Chong, S. H. Mellon, S. J. Tuck, Z. Q. Feng, J. M. Corey, and J. R. Chan, "A culture system to study oligodendrocyte myelination processes using engineered nanofibers," *Nat Methods*, vol. 9, no. 9, pp. 917–22, 2012. 1548-7105 Lee, Seonok Leach, Michelle K Redmond, Stephanie A Chong, S Y Christin Mellon, Synthia H Tuck, Samuel J Feng, Zhang-Qi Corey, Joseph M Chan, Jonah R R01 NS062796/NS/NINDS NIH HHS/United States NS062796-02/NS/NINDS NIH HHS/United States Journal Article Research Support, N.I.H., Extramural Research Support, Non-U.S. Gov't United States Nat Methods. 2012 Sep;9(9):917-22. doi: 10.1038/nmeth.2105. Epub 2012 Jul 15.

[7] B. M. E., B. Lauren, and ffrench Constant Charles, "Cns myelin sheath lengths are an intrinsic property of oligodendrocytes," *Current Biology*, vol. 25, no. 18, pp. 2411–2416, 2015.

[8] F. Mei, S. P. J. Fancy, Y. A. Shen, J. Niu, C. Zhao, B. Presley, E. Miao, S. Lee, S. R. Mayoral, S. A. Redmond, A. Etxeberria, L. Xiao, R. J. M. Franklin, A. Green, S. L. Hauser, and J. R. Chan, "Micropillar arrays as a high-throughput screening platform for therapeutics in multiple sclerosis," *Nat Med*, vol. 20, no. 8, pp. 954–960, 2014. 1546-170x Mei, Feng Fancy, Stephen P J Shen, Yun-An A Niu, Jianqin Zhao, Chao Presley, Bryan Miao, Edna Lee, Seonok Mayoral, Sonia R Redmond, Stephanie A Etxeberria, Ainhoa Xiao, Lan Franklin, Robin J M Green, Ari Hauser, Stephen L Chan, Jonah R F31 NS081905/NS/NINDS NIH HHS/United States Journal Article Research Support, Non-U.S. Gov't United States Nat Med. 2014 Aug;20(8):954-960. doi: 10.1038/nm.3618. Epub 2014 Jul 6.

[9] D. Espinosa-Hoyos, A. Jagielska, K. A. Homan, H. Du, T. Busbee, D. G. Anderson, N. X. Fang, J. A. Lewis, and K. J. Van Vliet, "Engineered 3d-printed artificial axons," *Sci Rep*, vol. 8, no. 1, p. 478, 2018. 2045-2322 Espinosa-Hoyos, Daniela Jagielska, Anna Homan, Kimberly A Du, Huifeng Busbee, Travis Anderson, Daniel G Fang, Nicholas X Lewis, Jennifer A Van Vliet, Krystyn J Journal Article England Sci Rep. 2018 Jan 11;8(1):478. doi: 10.1038/s41598-017-18744-6.

[10] O. Ronneberger, P. Fischer, and T. Brox, "U-net: Convolutional networks for biomedical image segmentation," Medical Image Computing and Computer-Assisted Intervention – MICCAI 2015, pp. 234–241, Springer International Publishing.

[11] P. N. Bullock and L. H. Rome, "Glass micro-fibers: a model system for study of early events in myelination," *J Neurosci Res*, vol. 27, no. 3, pp. 383–93, 1990. Bullock, P N Rome, L H HD 06576/HD/NICHD NIH HHS/United States Journal Article Research Support, U.S. Gov't, P.H.S. United States J Neurosci Res. 1990 Nov;27(3):383-93. doi: 10.1002/jnr.490270317.

[12] A. A. Jarjour, C. Manitt, S. W. Moore, K. M. Thompson, S.-J. Yuh, and T. E. Kennedy, "Netrin-1 is a chemorepellent for oligodendrocyte precursor cells in the embryonic spinal cord," *The Journal of Neuroscience*, vol. 23, no. 9, pp. 3735–3744, 2003.

[13] M. Abadi, A. Agarwal, P. Barham, E. Brevdo, Z. Chen, C. Citro, G. S. Corrado, A. Davis, J. Dean, M. Devin, S. Ghemawat, I. Goodfellow, A. Harp, G. Irving, M. Isard, R. Jozefowicz, Y. Jia, L. Kaiser, M. Kudlur, J. Levenberg, D. Mané, M. Schuster, R. Monga, S. Moore, D. Murray, C. Olah, J. Shlens, B. Steiner, I. Sutskever, K. Talwar, P. Tucker, V. Vanhoucke, V. Vasudevan, F. Viégas, O. Vinyals, P. Warden, M. Wattenberg, M. Wicke, Y. Yu, and X. Zheng., "Tensorflow: Large-scale machine learning on heterogeneous systems,," 2015.

[14] G. Bradski, "The opencv library," *Dr. Dobb's Journal of Software Tools*, 2000.

[15] P. Jaccard, "The distribution of the flora in the alpine zone.1," *New Phytologist*, vol. 11, no. 2, pp. 37–50, 1912.

[16] A. M. Krasnow, M. C. Ford, L. E. Valdivia, S. W. Wilson, and D. Attwell, "Regulation of developing myelin sheath elongation by oligodendrocyte calcium transients in vivo," *Nature Neuroscience*, vol. 21, no. 1, pp. 24–28, 2018.

[17] G. V. Michailov, M. W. Sereda, B. G. Brinkmann, T. M. Fischer, B. Haug, C. Birchmeier, L. Role, C. Lai, M. H. Schwab, and K.-A. Nave, "Axonal neuregulin-1 regulates myelin sheath thickness," *Science*, vol. 304, no. 5671, pp. 700–703, 2004.

[18] H. Wake, P. R. Lee, and R. D. Fields, "Control of local protein synthesis and initial events in myelination by action potentials," *Science*, vol. 333, no. 6049, pp. 1647–1651, 2011.

[19] H. Zhang, A. A. Jarjour, A. Boyd, and A. Williams, "Central nervous system remyelination in culture–a tool for multiple sclerosis research," *Exp Neurol*, vol. 230, no. 1, pp. 138–48, 2011. 1090-2430 Zhang, Hui Jarjour, Andrew A Boyd, Amanda Williams, Anna 083585/Wellcome Trust/United Kingdom Journal Article Research Support, Non-U.S. Gov't United States Exp Neurol. 2011 Jul;230(1):138-48. doi: 10.1016/j.expneurol.2011.04.009. Epub 2011 Apr 16.